Cooling rates dependence of medium-range order development in Cu_{64.5}Zr_{35.5} metallic glass

Y. Zhang, F. Zhang, C. Z. Wang, M. I. Mendelev, M. J. Kramer, and K. M. Ho

Phys. Rev. B **91**, 064105 — Published 23 February 2015

DOI: 10.1103/PhysRevB.91.064105

Cooling rates dependence of medium range order development in $Cu_{64.5}Zr_{35.5}$ metallic glass

Y. Zhang[1], F. Zhang[1], C.Z. Wang[1,2,*], M.I. Mendelev[1], M.J. Kramer [1,3] and K.M. Ho[1,2]

[1] *Ames Laboratory-USDOE, Iowa State University, Ames, Iowa 50011, USA*

[2] *Department of Physics and Astronomy, Iowa State University, Ames, Iowa 50011, USA*

[3] *Department of Materials Science and Engineering, Iowa State University, Ames, Iowa 50011, USA*

*wangcz@ameslab.gov

Abstract

The atomic structure of metallic glasses (MGs) plays an important role on their properties. Numerous molecular dynamics (MD) simulations have revealed the icosahedral short range order (ISRO) as a dominant motif in Cu-Zr metallic glasses. However, the cooling rates utilized in most of the MD simulations (usually on the order of $10^{10\text{-}13}$ K/s) can be too high to allow the structure to relax into the actual structures. By performing a long sub-T_g annealing of the $Cu_{64.5}Zr_{35.5}$ alloy model at 700 K up to 2.0 μs using MD simulations, we systematically address the evolution of medium range order (MRO) as the cooling rates in MD simulations approach the experimental cooling rates (usually $10^{3\text{-}6}$ K/s). By reducing the effective cooling rates to as low as 2.8×10^{7} K/s, we found a significant enhancement of the ISRO and Bergman-type MRO. Comparing to the widely used face-, edge- or vertex-sharing icosahedra, we propose that the Bergman-type MRO is a much more unambiguous metric to characterize the MRO in Cu-Zr MGs. By analyzing the network formed by interpenetrating icosahedra using the graphical theory, we show that the degree of interpenetration of the icosahedra centers increases with decreasing cooling rates. The network becomes aggressively assortative, indicating that higher degree nodes tend to cluster and form backbones in the MG. All these results show that the networks in the models prepared using lower cooling rates strongly deviate from a string-like morphology.

PACS number(s): 61.43.Dq, 61.43.Bn

I. Introduction

Metallic glasses (MGs) [1] represent an important family of new materials with extraordinary strengths and elasticity [2]. Understanding the structure-property relationship is a fundamental and central task in the research of MGs. Unlike crystalline materials, MGs do not have long-range translational order. However, various experiments [3,4] and computer simulations [5,6] have revealed short- to medium-range order in MGs. Here we define the short-range order (SRO) restricted to atomic arrangement within the first coordination shell. Starting with this description of the SRO, many models have been proposed to describe the medium-range order (MRO) in MGs [5,7,8].

As early as 1952, Frank proposed that icosahedra (ICO) was responsible for the large supercooling of metallic liquids observed experimentally [9]. ICO consists of twelve coordinated atoms and compose of twenty tetrahedral, which have energy 8.4% lower than the dense packed *fcc* or *hcp* clusters assuming Lennard-Jones interactions. The existence of icosahedral short range order (ISRO) in metallic liquids and MGs has been demonstrated by various experiments [4,10]. It has now been widely accepted that ISRO are dominant in many Cu-Zr MGs [11,12]. Many molecular dynamics (MD) simulations have revealed the close relationships (1) between ISRO and glass forming ability [11] and transport properties [13,14] in supercooled Cu-Zr liquids and (2) between ISRO and mechanical properties [15-17] in Cu-Zr MGs. Meanwhile, the MRO in Cu-Zr MGs has also been intensively investigated, where the population of interpenetrating, vertex-, edge- and face-sharing ICO has been analyzed [18-20]. The interpenetrating ICO has been identified as a major type MRO in Cu-Zr MGs [19]. The MRO formed by the interpenetrating ICO is believed to govern the mechanical response of the Cu-Zr MGs upon deformation [21]. However, characterization of the MRO in Cu-Zr MGs using different types of connections among ICO is still ambiguous, since one ICO can adopt many types of connections to a nearby ICO. Recently, the Bergman type MRO (BMRO) has been revealed as another key MRO in Cu-Zr MGs by our group [22]. The Bergman supercluster has three coordination shells with 45 atoms involved. The first shell is an

ICO (12 atoms), surrounded by a dodecahedron (20 atoms) and another ICO (12 atoms) as the second and third shell, respectively.

While dominant consensus is that the MRO is responsible for many unusual properties of Cu-Zr MGs, there is no clear understanding of how this complex MRO develops and what factors control its evolution during cooling. The MRO in MGs is difficult to decipher by microscopy or diffraction measurements. In particular the higher order correlations are lost when Fourier transforming the diffraction data to the pair-distribution functions. However, in supercooled Cu-Zr liquids both the sharpening of the diffuse scattering peak and splitting in the second peak observed by diffraction experiments have been correlated to enhanced MRO via MD simulations, where the cooling rate is not expected to be the dominant factor [23]. Even the recognition of SRO using nano-beam electron diffraction requires matching the experimental fingerprint from a local cluster to an atomic simulation model [24]. Most of the structure models for the MRO in MG so far are derived from MD simulations. For example, MRO in Cu-Zr MDs has been proposed to be a string-like network of interpenetrating ICOs [20,25]. However, such a MRO picture is questionable due to the ultrahigh cooling rates in the MD simulations (~10^{10} K/s or higher) compare to experimental cooling rates (usually on the order of 10^3 to 10^6 K/s). Therefore the MRO in a more stable glass after sufficient long time for relaxation needs to be further investigated.

Recently, annealing close to the glass transition (T_g) has been demonstrated to effectively reduce the effect of ultrahigh cooling rates used in MD simulations [26-28], which opens a door to investigate the development of MRO in a more stable glass. In the present study, we adopted a sub-T_g annealing at 700 K for 2.0 μs to reduce the effective cooling rates used to prepare $Cu_{64.5}Zr_{35.5}$ MGs in MD simulations. The lowest effective cooling rate can reach 2.8×10^7 K/s, which is about two orders of magnitude lower than conventional cooling rates used in MD simulations. As a result, the model prepared under lower effective cooling rates has a structure factor much closer to experimental results, indicating that the model catches the main structural features of real Cu-Zr MGs. The impact of lowering effective cooling rates on the evolutions of SRO and MRO was the

focus of the present study. It was found that the morphology of the network formed by interpenetrating ICO shows a significant deviation from a string-like pattern upon lowering the effective cooling rates. We also propose that the BMRO is a more unambiguous metric to characterize the MRO in Cu-Zr MGs than the conventionally used vertex-, edge- and face-sharing schemes.

The rest of the paper is organized as follows: the details of the MD simulation are described in section II. In section III, we first determine the effective cooling rates. Then the model prepared using the lowest effective cooling rate is validated by comparing the structure factor with experiments. The evolutions of SRO and MRO upon lowering the effective cooling rates are focused. Finally we adopt the graphical theory to shed more light on the nature of the network formed by interpenetrating ICO.

II. Simulation details

Classical MD simulations of $Cu_{64.5}Zr_{35.5}$ MGs were performed using the widely accepted Finnis-Sinclair type potential developed in [29]. Isothermal-isobaric ensemble (*NPT*, *N*=5000 atoms, *P*=0) and Nosé-Hoover thermostat were used throughout the sample preparation. The time step for integration was 2.5 fs. After a pre-equilibration at 2000 K, the model was continuously quenched down to 700 K under a cooling rate of 10^{10} K/s. Previous MD studies have revealed $T_g \approx 750$ K [22] using the same interatomic potential and cooling rate, therefore the as-quenched model is already in a glassy state. The as-quenched model was annealed isothermally at 700 K for 0.1, 0.5 and 2.0 μs, respectively, followed by a continuous cooling at 10^{10} K/s from 700 to 300 K. In order to demonstrate the effect of annealing on the effective cooling rates, we also prepared MD models using continuous cooling from 2000 to 300 K at 10^{13}, 10^{12}, 10^{11} and 10^{10} K/s, respectively.

In order to eliminate the effect of atomic thermal motions on local atomic structures, we collected 10,000 successive snapshots at 300 K to calculate the averaged atomic positions. All the analysis on the atomic structures in the following are carried out

using the averaged atomic positions. The cluster alignment method [30] was adopted to characterize the ISRO and BMRO. A cluster around each Cu atom is extracted from the averaged MD structure and aligned against an ideal 13-atom ICO or a 45-atom Bergman supercluster template. In real Cu-Zr MGs, the coordination shells of both ICO and Bergman superclusters are distorted due to different sizes of Cu and Zr atoms. Therefore the BMRO is regarded to be Bergman-type but may not be perfect Bergman superclusters. An alignment score is defined as follows to describe how the as-extracted cluster deviates from the template:

$$f = \left(\frac{1}{N}\sum_{i=1}^{N}|\boldsymbol{r}_{ic} - \boldsymbol{r}_{it}|^2\right)^{1/2}/r_0 \quad (1)$$

where f is the alignment score, N is the number of the atoms in the template, r_0 is the typical bond length of the template, $\boldsymbol{r}_{ic}$ and $\boldsymbol{r}_{it}$ are the atom positions in the aligned cluster and template, respectively. The smaller the alignment score is, the similar the cluster to the template in structure. We employed a cutoff score of 0.146 and 0.25 to identify the ISRO and Bergman-type MRO (BMRO) in this study, which is consistent with our previous studies [22,26].

III. Results and discussions

A. Determination of the effective cooling rates

The evolution of the instantaneous potential energy as a function of simulation time was present in Fig. 1(a). The decrease in the potential energy during annealing can be clearly observed. The total drop in potential energy after annealing at 700 K for 2.0 μs is about 10-15 meV/atom, which is more significant in t=0-0.9 μs. From t=0.9-2.0 μs the energy drops very slowly. As a result, an energetically more favorable glassy state has been achieved. The inherent structures were obtained by relaxation of the instantaneous atomic structures using a steepest descent method. The evolution of the energy of inherent structures is similar to the instantaneous potential energy. It shows that the model has visited many low energy meta-basins during annealing.

To determine the effective cooling rates by applying the long sub-T_g annealing, the potential energy of the models at T=300 K as a function of cooling rates was plotted in Fig. 1(b). A linear dependence of the potential energy on the logarithm of cooling rate

can be observed for the continuously cooled models. The potential energy decreases by 5-6 meV/atom as the cooling rate is lowered by an order of magnitude. Assuming this linear relationship persists for even lower cooling rates, extrapolation of the linear dependence yields effective cooling rates of 5.0×10^8, 6.3×10^7 and 2.8×10^7 K/s after annealing at 700 K for 0.1, 0.5 and 2.0 μs, respectively, which is much lower than the conventional cooling rates employed in MD simulations [19,27]. The total MD time interval needed to prepare a model at cooling rates of 2.8×10^7 K/s would be about 60.7 μs under continuously cooling. By applying the long sub-T_g annealing it can be achieved within 2.2 μs (cooling plus annealing). Therefore the long sub-T_g annealing at 700 K relaxes the glassy state more effectively, pushing the model much closer to realistic conditions of production of Cu-Zr MGs. In the following context, we will use the effective cooling rates to denote the models prepared by applying the sub-T_g annealing.

B. Comparison with experiments

We first set out to demonstrate that lowering the effective cooling rates can bring the atomic structures of the MD models closer to real MGs. The most straightforward and convenient metrics to compare the atomic structures between experiments and MD models is the total structure factor $S(Q)$. The total $S(Q)$ was calculated as follows: (1) the partial pair correlation functions $g_{ij}(r)$ (i and j denote type of atoms) were calculated using the atomic positions in the models; (2) $g_{ij}(r)$ were transformed into partial structural factors $S_{ij}(Q)$ using a Fourier transform:

$$S_{ij}(Q) = 4\pi\rho \int (g_{ij}(r) - 1)\frac{\sin(Qr)}{Q} r dr \qquad (2)$$

where the scattering vector $Q=4\pi sin\theta/\lambda$, with the 2θ *and* λ being the scattering angle and synchrotron wavelength, respectively, ρ is the number density of the relevant atom species; (3) the total $S(Q)$ were calculated using the weighted sum of the $S_{ij}(Q)$ obtained in step (2), *i.e.* $S(Q) = \sum_{i=1}^{2}\sum_{j\geq i}^{2} w_{ij}(Q) S_{ij}(Q)$, where $w_{ij}(Q)$ are the weighting factors for each $S_{ij}(Q)$ that are Q dependent in synchrotron diffraction.

The calculated $S(Q)$ from the MD models at T=300 K prepared using cooling rates of 10^{10} K/s and 2.8×10^7 K/s respectively are compared with the experimental $S(Q)$ reported in Ref [31] in Fig. 2. It can be seen that while the $S(Q)$ of both MD models agree

very well with the experiments, the agreement is even better at the lower cooling rate: (1) While the amplitude of the first peak centered at about 27 nm^{-1} from the model prepared at 10^{10} K/s is slightly lower than the experimental $S(Q)$, the height of this peak increases and matches the experimental $S(Q)$ very well at the effective cooling rate of 2.8×10^{7} K/s. Meanwhile a slight shift of the first peak towards high Q can be also observed. (2) The first minimum of S(Q) of the model prepared at 10^{10} K/s is higher than the experiment. However, the first minimum of S(Q) agrees with experiment very well when the effective cooling rates is lowered to 2.8×10^{7} K/s. (3) The amplitude of the second peak also increases upon lowering the effective cooling rate. All these cooling rate dependent trends correspond well to the experimental *in-situ* diffraction study of various MGs [23,32,33]. It can be seen that the MD model with the effective cooling rate of 2.8×10^{7} K/s indeed has atomic structure closer to real MGs.

C. Structural evolution upon lowering the cooling rates

1. Evolution of ISRO and MRO

The statistics of the structural characteristics for different effective cooling rates is summarized in Table I. The atomic structures were characterized in terms of ISRO using the fractions of the centers and total atoms involved in ISRO as metrics. It should be noted that all the identified centers of ICO are Cu atoms, while the Zr-centered cluster usually have a larger coordination number and are thus incompatible to icosahedral packing. It can be seen that all the metrics increase monotonously upon lowering the effective cooling rates. Only 8.1% of the Cu atoms are ICO centers under the cooling rate of 10^{13} K/s, whereas it increases drastically to 27.7% as the effective cooling rate drops to 2.8×10^{7} K/s. Correspondingly, the total atoms involved in ISRO have almost doubled in population, from 39.3% to 77.0%. These results clearly demonstrate the enhancement of ISRO upon lowering the effective cooling rates. A recent study [18] has reported a larger increase in the ICO after annealing a Cu-Zr MG at T=800 K using a different interatomic potential, which is consistent with our results. Nevertheless, whether the annealing leads to a structure closer to experiment was not reported.

The MRO in Cu-Zr MGs has been commonly characterized by the various types of connections among ICO [20]. If two ICO centers are not nearest neighbors of each other, but they share one, two or three common neighbor atoms, the types of connections are called vertex-, edge- or face-sharing, respectively. The change in the fractions of ICO connections under different cooling rates is demonstrated using the radial distribution function $G_c(r)=4\pi r^2\rho_c g_c(r)$ in Fig. 3(a), where $g_c(r)$ is the pair correlation function calculated only using the ICO centers and ρ_c is the number density of the ICO centers in the model. Four peaks can be clearly identified, especially in the models prepared using lower effective cooling rates. However, some care has to be taken when we assign the peaks of $G_c(r)$ to different connection types. In Fig. 3(b), the distributions of the distances between two ICO centers adopting each type of connection in the model with effective cooling rate of 2.8×10^7 K/s are shown. It can be seen that the first and second peaks centered at 0.27 and 0.44 nm correspond to the interpenetrating and face-sharing ICO, respectively, but the last two peaks in $G_c(r)$ do not have a one to one correspondence to the edge- and vertex-sharing. There is a considerable overlap between the histograms of edge- and vertex-sharing ICO at 0.5 nm. Therefore the peak centered at 0.51 nm is actually contributed by both edge- and vertex-sharing ICO. The amplitudes of all the peaks increase upon lowering the effective cooling rates, indicating that all the connection types are enhanced, which is in agreement with findings of Ref. [34]. However, an increase in the face-sharing connection at the expense of the edge-sharing [18] is not observed.

The BMRO has been recently proposed as a new tool to characterize to MRO in $Cu_{64.5}Zr_{35.5}$ MGs [22]. Instead of employing ICO as building units and focusing on the types of ICO connections, BMRO describes the architecture of MRO from the coordination shells in the Bergman superclusters. Similar to the statistics of ISRO, it can be seen from Table I that the population of BMRO centers also increases upon lowering the cooling rate, *i.e.* from 0.03% in the model cooled at 10^{13} K/s to 2.8% in the model under the effective cooling rate of 2×10^8 K/s. Correspondingly, atoms involved in BMRO increase dramatically from 6.7% to 60.1% of the total atoms in the simulation box. These results clearly demonstrate the enhancement of BMRO upon lowering the effective

cooling rates. The spatial distribution of the BMRO is shown in Fig. 4. The rapid increase in BMRO upon lowering the effective cooling rates can be clearly observed. Under high cooling rates (*e.g.* 10^{12} K/s) the BMRO is not only low in population but also spatially uncorrelated. However, BMRO can connect with each other to form a network as the effective cooling rates drops to 2×10^{8} K/s. Compared to the conventionally used vertex-, edge- and face-sharing schemes, the BMRO characterizes the MRO in Cu-Zr MGs much more unambiguously in terms of coordination shells.

2. Networks formed by interpenetrating ICO

Although the MRO described by the face-, edge- or vertex-sharing ICO provide details of ICO connections, these metrics are not convenient to characterize the MRO in Cu-Zr MGs. Because an ICO can adopt various types of connections with its nearby centers, its status is hard to be characterized unambiguously. Therefore, we prefer to adopt the networks formed by interpenetrating ICO as a metric to further investigate the MRO. The choice was made based on the following statistics.

Here we first analyze the bonding status of the ICO in terms of isolated and connected ICO. An isolated ICO do not share any of its constituent atoms with any other ICO. On the contrary, a connected ICO shares one or more its constituent atoms with a nearby ICO. The statistics of the ICO centers is present in Table II. It can be seen that ICO clusters tend to connect in all the models. Even under the fastest cooling of 10^{13} K/s 96.5% of the ICO centers are connected, where only very limited relaxation was allowed under this circumstance. The population of connected ICO centers increases upon decreasing the effective cooling rates. At 2.8×10^{7} K/s all the ICO centers are connected. Next we divided the connected ICO into two groups: interpenetrating and non-interpenetrating ICO. Two ICO centers are interpenetrating when they are nearest neighbor of each other (separation less than 0.3 nm as shown in Fig. 3). Non-interpenetrating ICO share some common atoms in the first coordination shell but do not share centers. It can be seen from Table II that 78.5% of the ICO centers have at least one interpenetrating connection even under the cooling rate of 10^{13} K/s. The population of ICO centers having interpenetrating connections increases significantly to 93.3% as the

effective cooling rate drops to 2.8×10^7 K/s. It implies that ICO are strongly correlated and aggregated into networks in space rather than randomly distributed. Moreover the interpenetrating ICO were reported to have lower energy than ICO connected via vertex-, edge- and face-sharing schemes [20]. Thus the networks formed by interpenetrating ICO reflect more intrinsic features of the MRO in Cu-Zr MGs.

The spatial distribution of the networks formed by interpenetrating ICO centers is shown in Fig. 5. It can be clearly seen that the networks form a string-like pattern under high cooling rates larger than 10^{10} K/s. Under extreme cooling rates (*e.g.* 10^{12} K/s) most of the strings are short in length and isolated in space. Nevertheless, the morphology of the networks exhibits a clear deviation from string-like as the effective cooling rate reduces to $10^{7\text{-}8}$ K/s, where the ICO centers interconnect with each other to develop a dense network.

In the following we adopt graphical theory to analyze the properties of the networks formed by interpenetrating ICO. Each ICO center is treated as a node of the networks. Two nodes are called connected if there is an interpenetrating connection between them. Each network comprise nodes satisfying the following criteria: (1) all the nodes in the same network are connected; (2) no connection can be found among different networks. Therefore each network represents a fragment composed by ICO. In the following, we will analyze the networks based on its connectivity, morphology and dimensionality as a function of the effective cooling rates.

We firstly characterize the statistics of the networks, *i.e.* how many networks can be found in the models and how many nodes the largest network has. The upper limit of the number of networks is the number of nodes (N_{node}), if there is no connection between any nodes. As a result all the networks will have only one node. On the contrary, if all the nodes are connected, there will be only one network which contains N_{node} nodes. The number of networks and the number of nodes in the largest network as a function of effective cooling rates are listed in Table III. The results are normalized using the total number of nodes (ICO centers). It can be seen that there are many networks (38% of the

upper limit), but the largest network only has 8% of the total nodes under the cooling rate of 10^{13} K/s. The total number of network decreases while the number of nodes involved in the largest network increases as the effective cooling rate is lowered. As a contrast, the number of network is only 4% of the upper limit and the largest network contains 91% of the total nodes under the effective cooling rate of 2.8×10^{7} K/s. These results clearly reflect the growth of the network formed by ICO centers upon lowering the effective cooling rates.

Next we analyzed the degree of each node (N_c). The degree of a node is defined as the total number of interpenetrating connections to the node. Fig. 6 shows the populations of nodes with degree from zero (non-interpenetrating ICO) to six (highly interpenetrated ICO) in all the models at 300 K prepared using various effective cooling rates. Several features can be observed: (1) nodes with N_c=1 are the most abundant at the cooling rate of 10^{13} K/s, indicating a very low degree of interpenetration among the ICO centers due to the fast cooling; (2) Under the cooling rate from 10^{11} to 5.0×10^{8} K/s, nodes with N_c=2 become the most popular; (3) Nodes with N_c=3 are the most abundant when the effective cooling rate is lower than 6.3×10^{7} K/s. All these results indicate an increasing degree of interpenetration among the ICO centers as extended time window for structural development is provided. It can be seen that nodes with $N_c\geq3$ significantly increase as the effective cooling rates are lowered. These nodes can serve as "hubs" in the networks formed by ICO centers, which promote the densification of the networks. As a result the morphology of the network will deviate strongly from string-like. The transition in the network morphology can be further reflected by calculating its assortativity coefficient [35]. A network is called assortative if the nodes with high N_c tend to aggregate. If the nodes with high N_c tend to connect with nodes with low N_c the network is called disassortative. If M is the number of edges, and for each edge i, x_i and y_i are the degrees of the nodes at either ends of edge i, the assortative coefficient (r_a) is defined by the following equation:

$$r_a = \frac{M^{-1}\sum_i x_i y_i - \left[M^{-1}\sum_i \frac{1}{2}(x_i+y_i)\right]^2}{M^{-1}\sum_i \frac{1}{2}(x_i^2+y_i^2) - \left[M^{-1}\sum_i \frac{1}{2}(x_i+y_i)\right]^2} \quad (i = 1, 2, \ldots, M) \qquad (2)$$

The range of the r_a values is between -1 and +1, where r_a=-1 corresponds to a completely disassortative network whereas r_a=-1 indicates a completely assortative network. The assortative coefficient as a function of effective cooling rates is present in Table III. It can be seen that r_a of all the models is positive, indicating the assortative nature of the network formed by the interpenetrating ICO. r_a increases from 0.282 to 0.443 as the effective cooling rate decreases from 10^{13} to 2.8×10^{7} K/s. It clearly shows that the nodes with high N_c tend to clustering and form a densely interpenetrated network.

The dimensionality of the networks (d) is defined by the relation of $N_d \sim L^d$, where N_d is the number of nodes in the network, L is a characteristic length of the network defined as the maximum among the topologically shortest paths between all node pairs [31]. The logarithm dependence of N_d on the logarithm of L in all the models prepared using different effective cooling rates is plotted in Fig. 7. Two linear regimes can be clearly observed in the log(L) ranging from 0.2 to 1.1 and from 1.1 to 1.8, respectively. The slope in the log(L) range of 0.2 to 1.1 is very close to unity. Previous study using a Cu-Zr model constructed by reverse Monte Carlo simulations revealed d=1.01 [31]. The d value close to unity indicates a string-like morphology of the network formed by the interpenetrated ICO centers, where L is almost proportional to the number of ICO centers in the network. It can be derived that networks composed of less than 20-25 ICO centers prefer a string-like pattern. Nevertheless, networks containing more than 100 ICO centers emerge as the effective cooling rates drop below 10^{10} K/s. These networks have a larger slope on the log(N_d)-log(L) plot close to 2, indicating a clear deviation from string-like networks in morphology. These results show that the morphology of the network formed by interpenetrating ICO centers is strongly dependent on the effective cooling rates. Lowering the cooling rates toward experimental values will drive the network to be more deviated from string-like.

D. Dependence of chemical ordering on effective cooling rates

Besides topological orders we also investigated the chemical ordering in the models at 300 K prepared using various effective cooling rates. The Cu concentrations in both the ISRO and BMRO are listed in Table I. It can be seen that the Cu concentrations in

both the ISRO and BMRO increase as the effective cooling rate is lowered. However, they are both lower that the nominal composition c_{Cu}=0.645, indicating the enrichment of Zr in both ISRO and BMRO in Cu-Zr MGs. When the effective cooling rate is larger than 10^{12} K/s, the Cu concentration in ISRO is higher than in BMRO. At the cooling rate of 10^{11} K/s ISRO and BMRO have almost the same composition of c_{Cu}=0.60. Nevertheless, BMRO has a higher Cu concentration as the effective cooling rates drops below 10^{11} K/s. Because BMRO composes a high degree of interpenetrating ICO, an enhancement in BMRO under lower effective cooling rates will promote a higher Cu concentration in BMRO. We further classified ICO in the models according to their stoichiometry (see Fig. 8). Under the cooling rates above 10^{12} K/s, Cu_8Zr_5 is the most abundant type. However, Cu_7Zr_6 becomes dominant as the cooling rate decreases, followed by Cu_6Zr_7 and Cu_8Zr_5, which is agreement with previous studies [36]. It can be seen that ICO with local chemistry of Cu_6Zr_7, Cu_7Zr_6 and Cu_8Zr_5 increase upon lowering the cooling rates, while the other types have undergone only slightly change. Actually the local chemistry of ICO is strongly correlated with not only chemical interactions but also topological constraint. Due to the mismatch between Cu and Zr atoms in size, having too many Zr atoms in the nearest neighbor will result in significant distortions [7], while having too many Cu atoms is not favored due to the large negative heat of mixing between Cu and Zr [37]. Here the enhancement of ICO with relative Cu-rich stoichiometry of Cu_7Zr_6, Cu_8Zr_5 will significantly promote the formation of BMRO.

IV. Conclusions

In this work, we performed a long annealing up to 2.0 μs at 700 K to reduce the effect of ultrafast cooling rates used in MD simulations. The effective cooling rate reached in our simulation is 2.8×10^7 K/s, which is about two orders of magnitude lower than conventional cooling rates employed in other MD simulations. The structure factor of the annealed model is closer to the experimental result, indicating the atomic structure in the model after annealing is much closer to the real $Cu_{64.5}Zr_{35.5}$ MG. The effects of cooling rate on the atomic structures and the evolution of SRO and MRO under different cooling rate are investigated. Both the icosahedral SRO and Bergman type MRO enhance

significantly upon lowering the cooling rate. It is shown that the BMRO is a more unambiguous metric to characterize the MRO in Cu-Zr MGs than the conventionally used vertex-, edge- and face-sharing schemes. The compositions of icosahedral SRO and Bergman type MRO are both Cu-rich, however, the Cu concentration in Bergman type MRO is much closer to the nominal composition than icosahedral SRO. The network formed by interpenetrating icosahedra is analyzed using the graphical theory. It is found that the degree of the nodes formed by icosahedra centers increases under slow cooling. The network becomes progressively assortative, indicating the aggregation of ICO centers with larger number of bonds to form backbones of the MG. While the string-like pattern has been often observed under high cooling rates in many MD simulations, our results suggest that the network will significantly deviate from a string-like pattern as the effective cooling rate approaches the experimental values.

Acknowledgements

This work was supported by the U.S. Department of Energy, Office of Basic Energy Science, Division of Materials Sciences and Engineering, including the computer time allocations at the National Energy Research Scientific Computing Center (NERSC) in Berkeley, CA. The research was performed at the Ames Laboratory. Ames Laboratory is operated for the U.S. Department of Energy by Iowa State University under Contract No. DE-AC02-07CH11358.

References

[1] A. Inoue, Acta Mater. **48**, 279 (2000).
[2] C. A. Schuh, T. C. Hufnagel, and U. Ramamurty, Acta Mater. **55**, 4067 (2007).
[3] K. Kelton, G. Lee, A. Gangopadhyay, R. Hyers, T. Rathz, J. Rogers, M. Robinson, and D. Robinson, Phys. Rev. Lett **90**, 195504 (2003).
[4] T. Schenk, D. Holland-Moritz, V. Simonet, R. Bellissent, and D. M. Herlach, Phys. Rev. Lett **89**, 075507 (2002).
[5] H. W. Sheng, W. K. Luo, F. M. Alamgir, J. M. Bai, and E. Ma, Nature **439**, 419 (2006).
[6] P. Guan, T. Fujita, A. Hirata, Y. Liu, and M. Chen, Phys. Rev. Lett **108**, 175501 (2012).
[7] D. B. Miracle, Acta Mater. **54**, 4317 (2006).
[8] D. B. Miracle, Nat. Mater. **3**, 697 (2004).
[9] F. C. Frank, P. Roy. Soc. Lond. A Mat. **215**, 43 (1952).
[10] Y. T. Shen, T. H. Kim, A. K. Gangopadhyay, and K. F. Kelton, Phys. Rev. Lett **102**, 057801 (2009).
[11] Z. D. Sha, Y. P. Feng, and Y. Li, Appl. Phys. Lett. **96**, 061903 (2010).
[12] Y. Q. Cheng, E. Ma, and H. W. Sheng, Phys. Rev. Lett **102**, 245501 (2009).
[13] H. L. Peng, M. Z. Li, W. H. Wang, C. Z. Wang, and K. M. Ho, Appl. Phys. Lett. **96**, 021901 (2010).
[14] Y. Zhang, N. Mattern, and J. Eckert, J. Appl. Phys. **110** (2011).
[15] Y. Q. Cheng, A. J. Cao, H. W. Sheng, and E. Ma, Acta Mater. **56**, 5263 (2008).
[16] Y. Q. Cheng and E. Ma, Acta Mater. **59**, 1800 (2011).
[17] Y. Q. Cheng, H. W. Sheng, and E. Ma, Phys. Rev. B **78**, 014207 (2008).
[18] J. Ding, Y.-Q. Cheng, and E. Ma, Acta Mater. **69**, 343 (2014).
[19] R. Soklaski, Z. Nussinov, Z. Markow, K. F. Kelton, and L. Yang, Phys. Rev. B **87**, 184203 (2013).
[20] M. Lee, C.-M. Lee, K.-R. Lee, E. Ma, and J.-C. Lee, Acta Mater. **59**, 159 (2011).
[21] A. J. Cao, Y. Q. Cheng, and E. Ma, Acta Mater. **57**, 5146 (2009).
[22] X. W. Fang, C. Z. Wang, S. G. Hao, M. J. Kramer, Y. X. Yao, M. I. Mendelev, Z. J. Ding, R. E. Napolitano, and K. M. Ho, Sci. Rep. **1**, 194, 194 (2011).
[23] M. I. Mendelev *et al.*, Philos. Mag. **90**, 3795 (2010).
[24] A. Hirata, P. Guan, T. Fujita, Y. Hirotsu, A. Inoue, A. R. Yavari, T. Sakurai, and M. Chen, Nat. Mater. **10**, 28 (2011).
[25] M. Wakeda and Y. Shibutani, Acta Mater. **58**, 3963 (2010).
[26] F. Zhang, M. I. Mendelev, Y. Zhang, C.-Z. Wang, M. J. Kramer, and K.-M. Ho, Appl. Phys. Lett. **104**, 061905 (2014).
[27] L. Ward, D. Miracle, W. Windl, O. N. Senkov, and K. Flores, Phys. Rev. B **88**, 134205 (2013).
[28] J. Ding, Y. Q. Cheng, and E. Ma, Appl. Phys. Lett. **101**, 121917 (2012).
[29] M. I. Mendelev, M. J. Kramer, R. T. Ott, and D. J. Sordelet, Philos. Mag. **89**, 109 (2009).
[30] X. W. Fang, C. Z. Wang, Y. X. Yao, Z. J. Ding, and K. M. Ho, Phys. Rev. B **82**, 184204 (2010).
[31] M. Li, C. Z. Wang, S. G. Hao, M. J. Kramer, and K. M. Ho, Phys. Rev. B **80**, 184201 (2009).
[32] N. Mattern, H. Hermann, S. Roth, J. Sakowski, M. P. Macht, P. Jovari, and J. Z. Jiang, Appl. Phys. Lett. **82**, 2589 (2003).
[33] N. Mattern, A. Schops, U. Kuhn, J. Acker, O. Khvostikova, and J. Eckert, J. Non-cryst. Solids **354**, 1054 (2008).
[34] M. Shimono and H. Onodera, Mater. Sci. Forum **539-543**, 2031 (2007).

[35] G. A. Pavlopoulos, M. Secrier, C. N. Moschopoulos, T. G. Soldatos, S. Kossida, J. Aerts, R. Schneider, and P. G. Bagos, Biodata Min. **4** (2011).
[36] Z. D. Sha, B. Xu, L. Shen, A. H. Zhang, Y. P. Feng, and Y. Li, J. Appl. Phys. **107**, 063508 (2010).
[37] A. Takeuchi and A. Inoue, Mater. Trans. **46**, 2817 (2005).

Figures

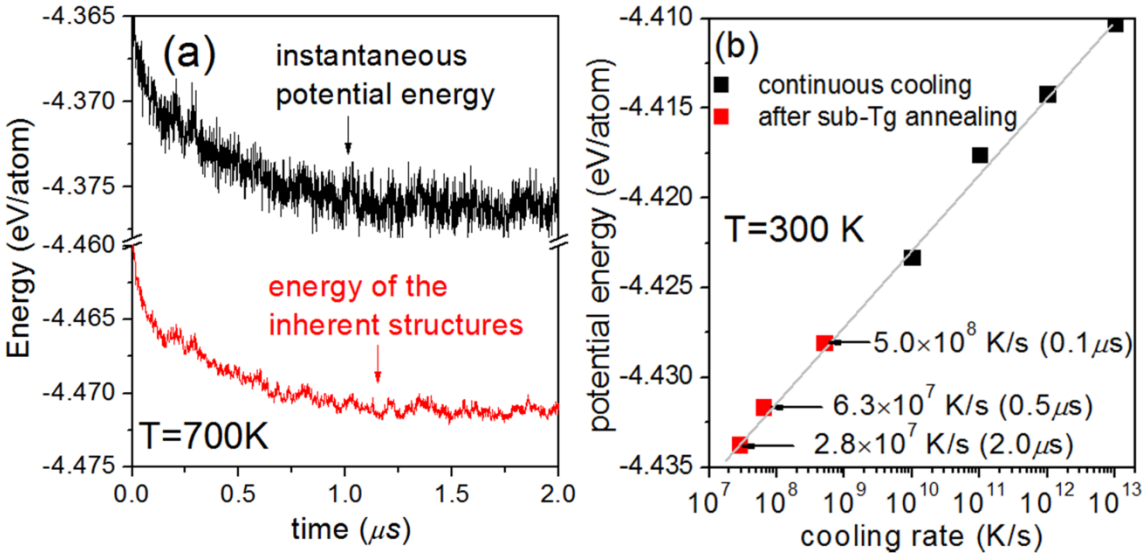

Fig. 1 (a) The evolutions of the instantaneous potential energy and energy of the inherent structures as a function of simulation time. (b) Potential energy of the models at 300 K as a function of cooling rates, the solid line indicates a linear fitting.

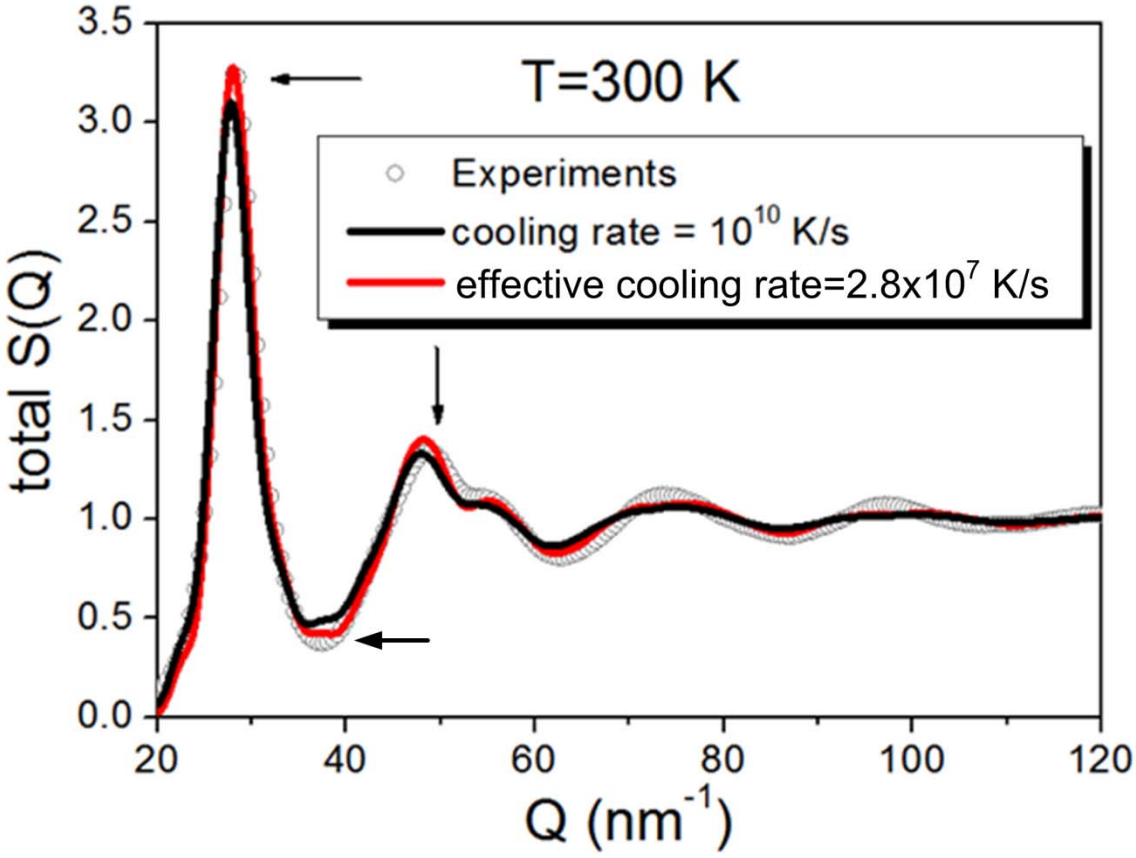

Fig. 2 The total structure factor of the MD models at 300 K with continuous cooling rate of 10^{10} K/s and effective cooling rate of 2.8×10^{7} K/s, respectively. The experimental S(Q) (open symbols) at 300 K is taken from Ref [32].

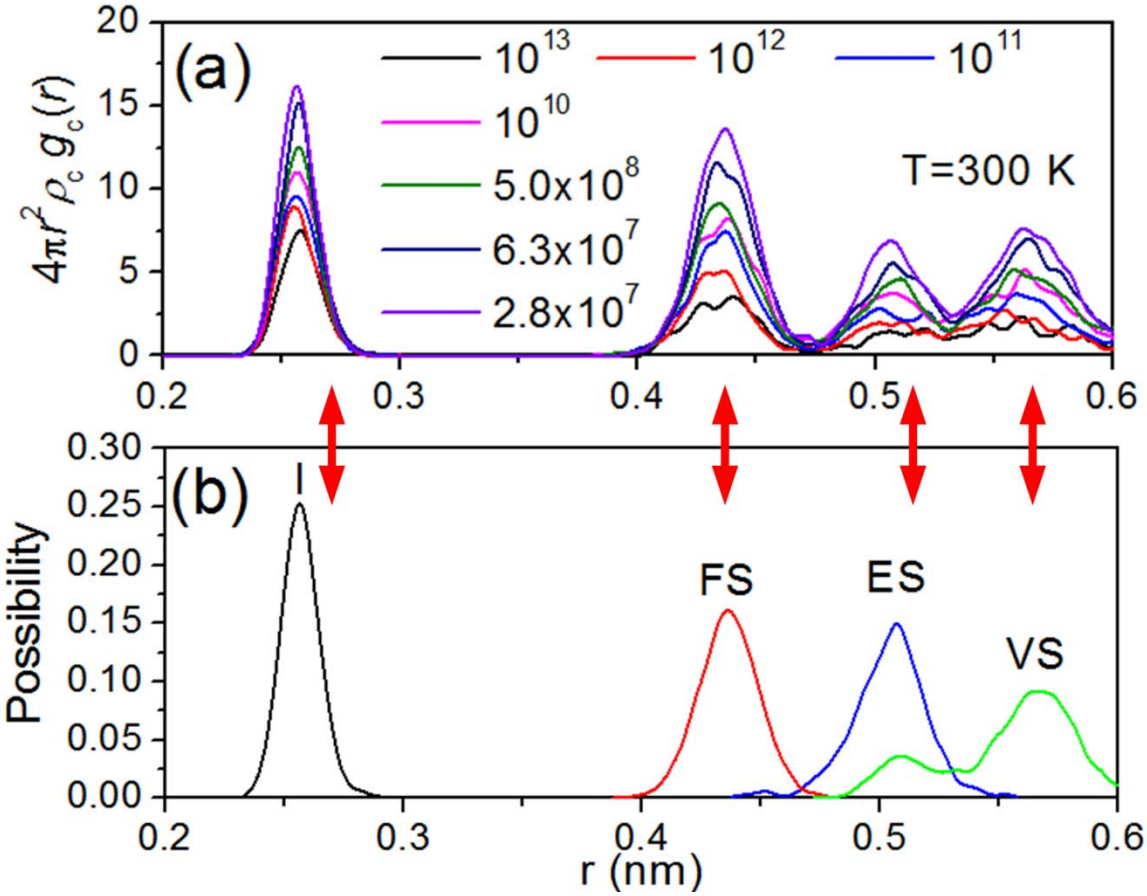

Fig. 3 (a) The radial distribution function $G_c(r)=4\pi r^2\rho_c g_c(r)$ calculated using only the icosahedral centers in models prepared using various effective cooling rates. (b) The distributions of the distance between two ICO centers adopting each type of connection in the model prepared using effective cooling rate of 2.8×10^7 K/s.

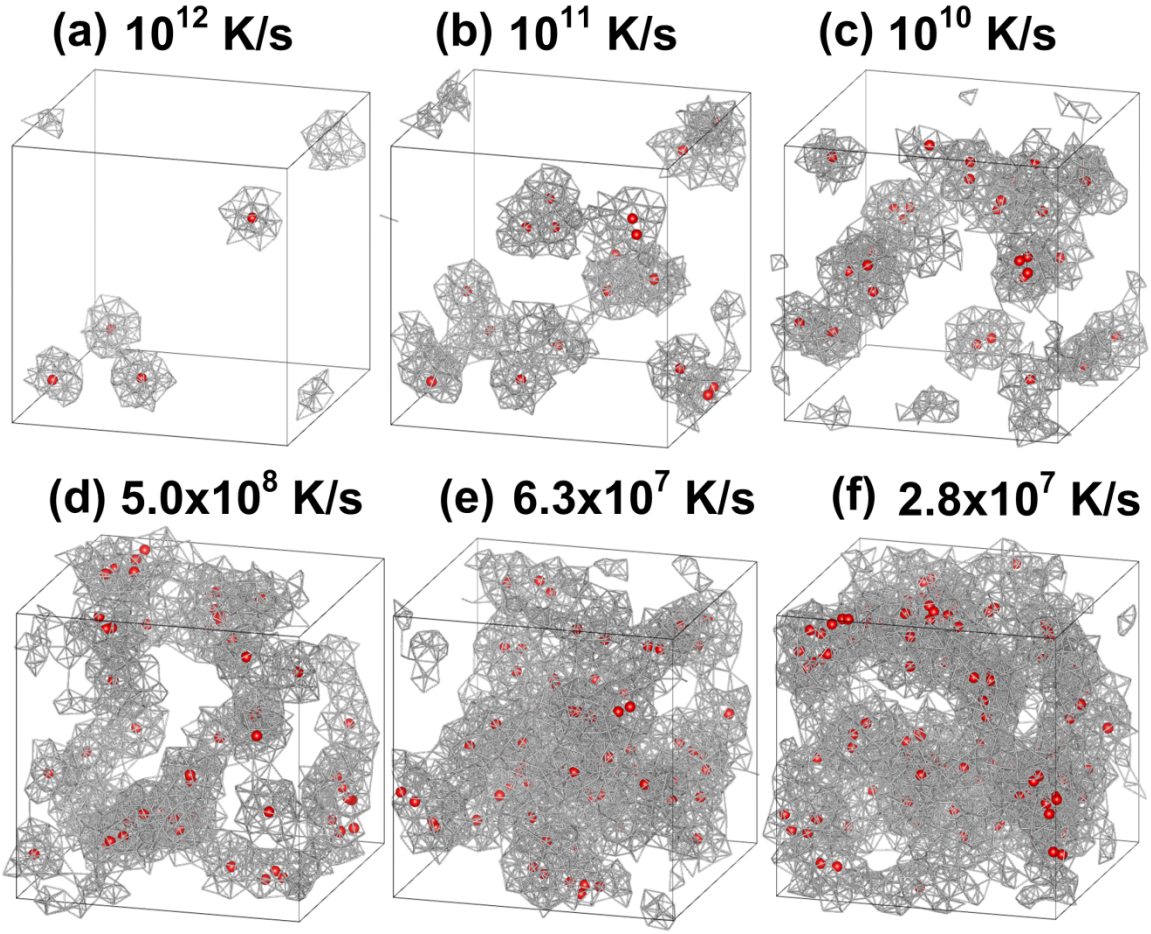

Fig. 4 Spatial distribution of the centers of Bergman superclusters at T=300 K in models prepared under effective cooling rates of (a) 10^{12}, (b) 10^{11}, (c) 10^{10}, (d) 5.0×10^{8}, (e) 6.3×10^{7} and (f) 2.8×10^{7} K/s, respectively. The centers of Bergman superclusters are plotted as the red atoms, whereas the other atoms involved are connected using bonds.

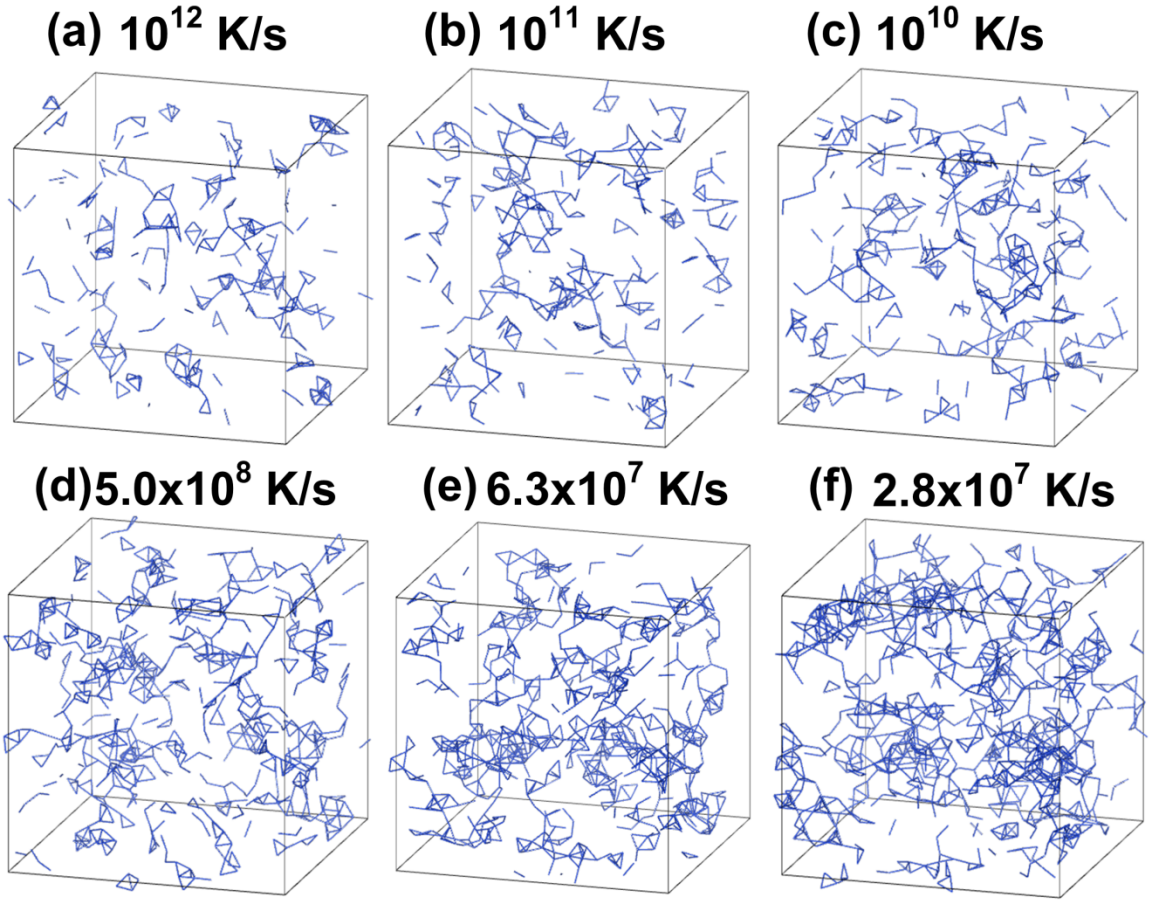

Fig. 5 Spatial distribution of the networks formed by interpenetrating ICO at T=300 K in models prepared under effective cooling rates of (a) 10^{12}, (b) 10^{11}, (c) 10^{10}, (d) 5.0×10^{8}, (e) 6.3×10^{7} and (f) 2.8×10^{7} K/s, respectively. A bond is drawn between the ICO centers with distances shorter than 0.3 nm.

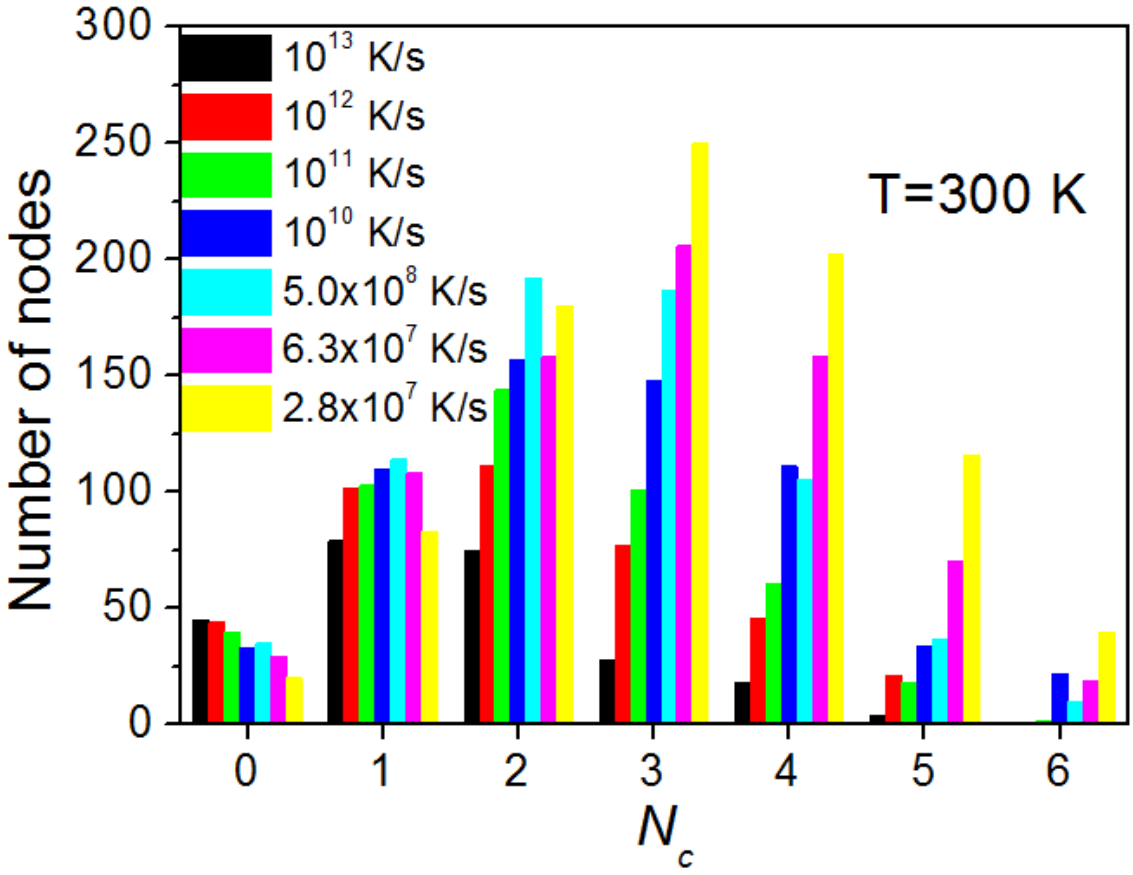

Fig. 6 The populations of nodes with degree from zero (non-interpenetrating ICO) to six (highly interpenetrated ICO) in models at T=300 K prepared under various effective cooling rates.

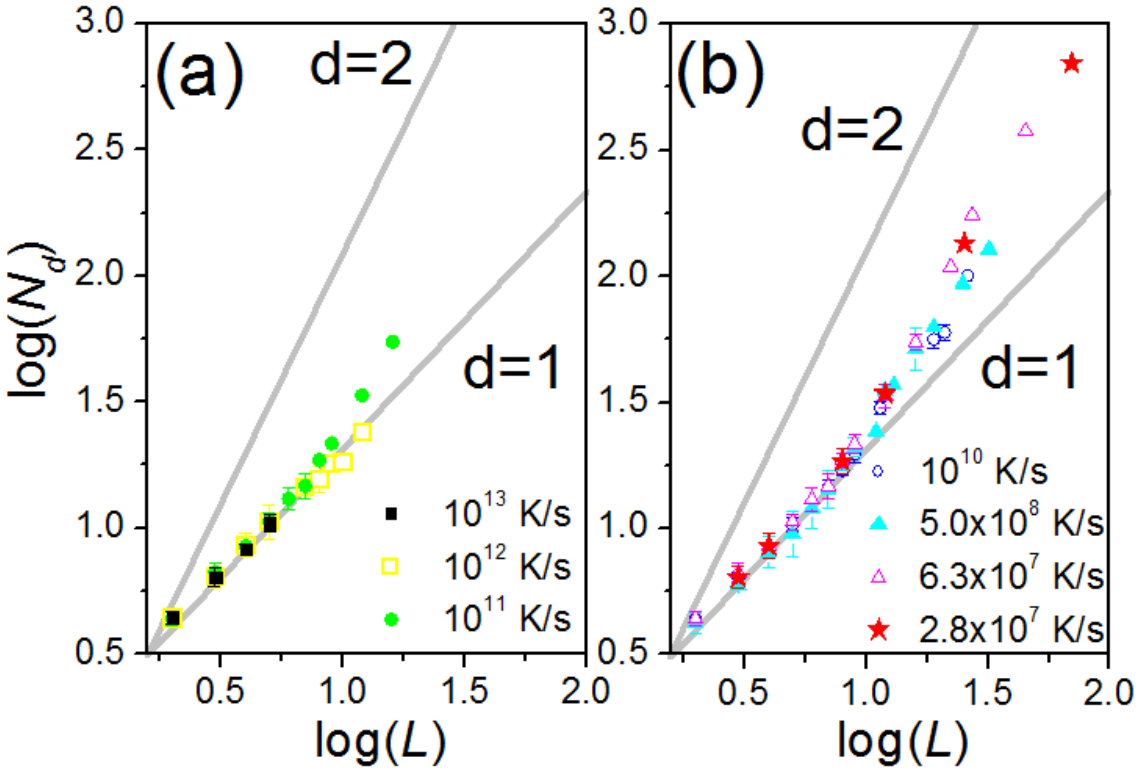

Fig. 7 The logarithm of the number of nodes in the networks (N_d) as a function of logarithm of shortest paths (L) in the models at 300 K prepared using different effective cooling rates.

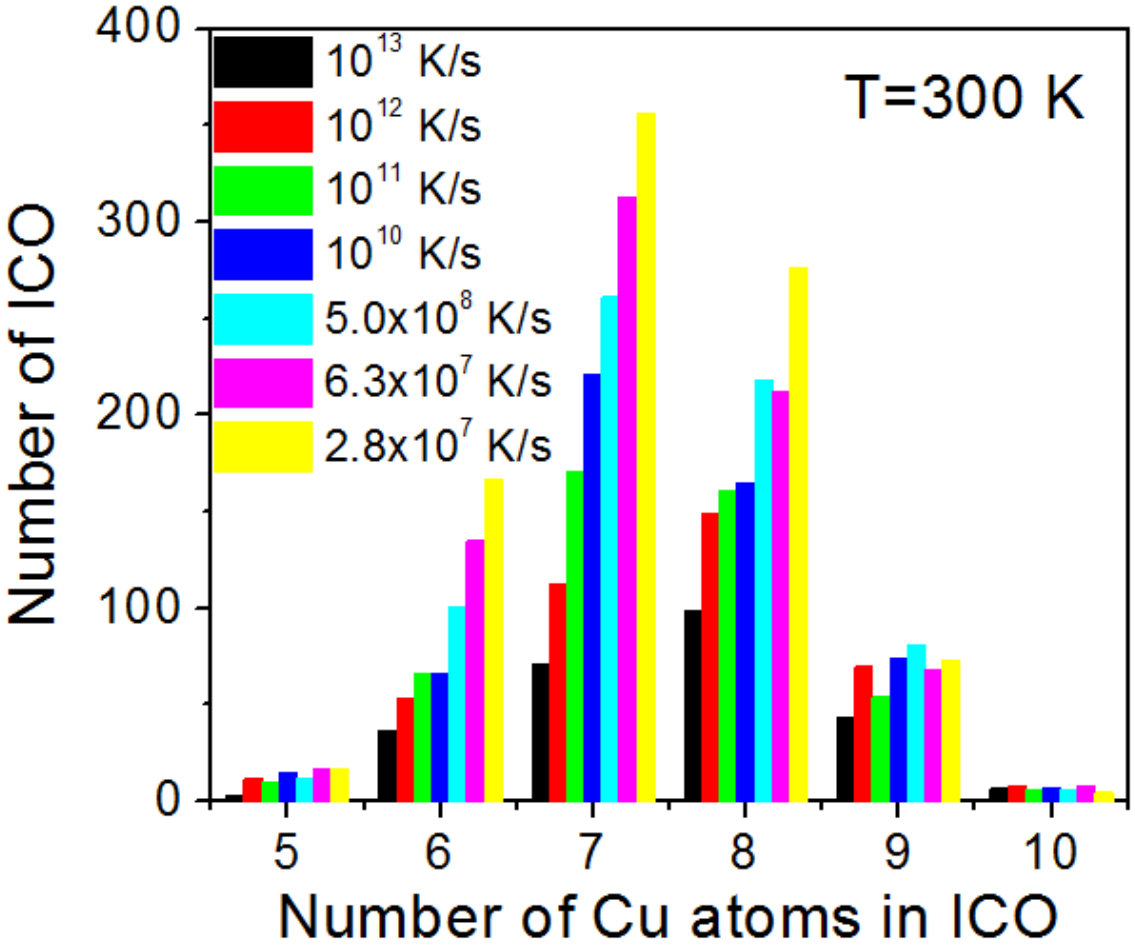

Fig. 8 The number of ICO with different stoichiometry (the central Cu atom is included) in models at T=300 K prepared under various effective cooling rates.

Tables

Table I The percentages of centers of ISRO (f_{Ic}) and BMRO (f_{Bc}), respectively, normalized using the total number of Cu atoms in the model. The percentages of atoms involved in ISRO (f_{Ia}) and BMRO (f_{Ba}), respectively, normalized using the total number of atoms in the model. The Cu concentration of the ISRO and BMRO, respectively, in the models prepared using various effective cooling rates. The nominal Cu concentration in all the models is 0.645.

Effective Cooling rate (K/s)	f_{Ic} (%)	f_{Ia} (%)	f_{Bc} (%)	f_{Ba} (%)	c_{Cu} in ISRO	c_{Cu} in BMRO
10^{13}	8.1	39.3	0.03	6.7	0.596	0.578
10^{12}	10.6	47.5	0.1	8.2	0.598	0.588
10^{11}	13.5	55.2	0.4	19.6	0.600	0.601
10^{10}	17.2	62.1	1.2	30.4	0.603	0.607
5.0×10^{8}	18.9	67.0	1.8	45.3	0.604	0.612
6.3×10^{7}	23.1	71.2	2.1	56.4	0.608	0.617
2.8×10^{7}	27.7	77.0	2.8	60.1	0.613	0.621

Table II The percentages of isolated (f_{iso}) and connected (f_{conn}, via face-, edge- and vertex- sharing or interpenetrating schemes) ICO centers, the fractions of ICO centers with at least one interpenetrating connection (f_{interp}) in the models prepared under different effective cooling rates. All the populations are normalized using the total number of ICO centers.

Effective Cooling rate (K/s)	f_{iso} (%)	f_{conn} (%)	f_{interp} (%)
10^{13}	3.4	96.5	79.3
10^{12}	1.5	98.5	83.2
10^{11}	1.1	99.1	87.0
10^{10}	0.16	99.8	88.7
5.0×10^{8}	0.15	99.8	89.3
6.3×10^{7}	0.11	99.9	90.0
2.8×10^{7}	0	100	93.3

Table III The number of networks (N_{net}) and the number of nodes in the largest network (N_{lnet}) in the models prepared using different effective cooling rates. The results are normalized using the total number of nodes (ICO centers). The assortative coefficients (r_a) are also present.

Effective Cooling rate (K/s)	N_{net}	N_{lnet}	r_a
10^{13}	0.38	0.08	0.282
10^{12}	0.26	0.07	0.307
10^{11}	0.21	0.12	0.321
10^{10}	0.14	0.20	0.343
5.0×10^{8}	0.13	0.25	0.374
6.3×10^{7}	0.09	0.38	0.407
2.8×10^{7}	0.04	0.91	0.443